MEDICAL IMAGE MEASUREMENT AND CHARACTERIZATION: EXTRACTING MECHANICAL AND THERMAL STRESSES FOR SURGERY

Aimé Lay-Ekuakille[1], Moise Avoci Ugwiri[2], Consolatina Liguori[2], Satya P. Singh[3], Md Zia Uhr Rahman[4], Domenico Veneziano[5]

1) *University of Salento, Department of Innovation Engineering, Via Monteroni sn, 73100 Lecce, Italy* (✉ *aime.lay.ekuakille@unisalento.it,* +39 0832 297 821)

2) *University of Salerno, Department of Industrial Engineering, Via Giovanni Paolo II n.132, 84084 Fisciano, Italy* (*mavociugwiri@unisa.it, tliguori@unisa.it*)

3) *Nanyang Technological University, School of Computer Science and Engineering, 50 Nanyang Ave, Singapore 639798 (satya@ntu.edu.sg)*

4) *K L University, Department of Electronics & Communication Engineering, Green Fields, Vaddeswaram, Guntur-522502, India (mdzr55@gmail.com)*

5) *Asl Reggio Calabria, Hospital "Bianchi-Melacrino-Morelli", Via Giuseppe Melacrino n.21, 89124 Reggio Calabria, Italy (info@domenicoveneziano.it)*

Abstract

Whatever the type of surgery related to inner organs, traditional or robotic, the contact with them during surgery is a key moment for pursuing the intervention. Contacts by means of surgery instruments namely scalpels, staples, clamps, graspers, etc. are decisive moments. False, and erroneous touching and manoeuvring of organs operated on can cause irreversible damage as regard morphological aspects (outer impact) and physiological aspects (inner impact). The topic is a great challenge in the effort to measure and characterize damages. In general, electrical instruments for surgery employ the following technologies: ultrasound, radiofrequency (monopolar, and bipolar), and laser. They all result in thermal damages difficult to evaluate. The article proposes a method for a pre-screening of organ features during robotic surgery sessions by pointing out mechanical and thermal stresses. A dedicated modelling has been developed based on experimental activities during surgery session. The idea is to model tissue behaviour from real images to help surgeons to be aware of handling during surgery. This is the first step for generalization by considering the type of organ. The measurement acquisitions have been performed by means of an advanced external camera located over the surgery quadrant. The modelling and testing have been carried out on kidneys. The modelling, carried out through Comsol Multiphysics, is based on the bioheat approach. A further comparative technique has been implemented. It is based on computer vision for robotics. The findings of human tissue behavior exhibit reliable results.

Keywords: infrared imaging, robotic surgery, imaging for cancer detection, bioinstrumentation, laparoscopy, biomedical measurements, biomechanical and stress.

1. Introduction

Human organs, in general, and human tissue, in particular, in the case of surgery are subject to heat and mechanical stress transfers. Certainly, there are different instrumental and analytic techniques that may allow to know organ and tissue stiffness and heat [1]. However, these techniques are generally noninvasive, except biopsy. Biopsy is a direct contact with the organ to be characterized through histological analysis [2]. But the scope of the biopsy is not to fix the issue by means of surgery but only to take some tissues for characterization. Hence, it is an invasive method but not allowing to directly know the stress in real time. Moreover, during surgery surprises can come forward especially in the case of tumor removal. Tissues of organs change under heat and mechanical stress and this can alter the goals of the intervention. There is a gap, then uncertainty, between surgery prediction before the activity begins and the real post-surgery activity. That is why, to avoid negative reactions and unpredicted avalanche effects, a modeling of surgery organ behavior is recommended. This kind of modeling falls within the scope of surgery preparation with or without AVR (*augmented virtual reality*). Surgeons usually do that regardless of the objective of this paper. During surgery, tissues are manipulated by means of graspers made of metal, namely steel, that renders them stiffer than the organs and the tissues under manipulation [3]. Damages, on tissue, produced by surgical instruments are reported in many studies [4]; others have developed methods for knowing errors in tissue injury due to graspers that reach 66% of all total cases in laparoscopic cholecystectomies including 13% related to exaggerated force [5]. As consequences, different researches have been implemented to optimize design and fabrication of graspers. In addition, modeling, as reported before, is mandatory to assess stresses from the thermal and mechanical viewpoint to avoid trauma with new a approach of grasper design and fabrication [6–8]. The key issue now is to know in advance the right load exerted by surgical instruments on the human tissue. Surgeons have difficulties to regulate the correct pressure; they need to define, for each organ, an optimal load volume to protect organ tissue against trauma [9]. Anyway, image capturing remains the best way to acquire information from the surgical field regardless the technology [10]. Mechanical stresses in living tissue [11], with impact at cellular and subcellular context, can be determined with 2D traction force microscopy, micropillar arrays, monolayer stress microscopy and monolayer stretching between flexible cantilevers. Traction force microscopy with 3D is also available. For *in vivo* approach, the techniques generally used are based on deformable inclusions, laser ablation and luminal pressure. From a general viewpoint, mechanical stress characterization, in a quantitative manner, takes place according to classes related to cells and tissues: kinematics and rheology [12–14]. Moreover, we can summarize all different techniques connected to mechanical stress in Table 1 [15].

There is no real time technique for measuring organ stress during the surgery; it is generally a delayed analysis taking time from 30 minutes up to 2 hours in case of complicated situations. A combination of an image-processing technique along with a camera and the cell element method based on the finite element method makes it possible to provide the calculated stresses as the loads apply [16]. But as reported in this paper, thermal stress is easier to verify in quasi-real time than the mechanical one thanks to the infrared camera, but the analysis is always delayed, though for a much shorter time than in the case of the mechanical stress. The paper illustrates the application of the concepts above on organ surgery, in particular, for the case of the kidneys. Kidneys are paired bean-shaped organs located on either side of the spine in the upper part of the abdomen. Each kidney is connected to the aorta and the vena cava by a single renal artery and vein. By means of these blood vessels, the kidneys filter around 1200 mL/min of blood. Each kidney consists of approximately a million of microscopic units denoted as nephrons

Table 1. Summary of technique comparisons.

	Measured quantities	Measurable range	Time scale*	Size scale**	Advantages	Disadvantages
Optical/magnetic tweezers	Cell junction tension	pN–nN	ms–min	0.1−10 μm	Non-contact Absolute measurements	Requires different control constructs, delicate calibration
FRET force probe	Intramolecular	pN	> s	nm	Molecular measurements	Requires different control constructs; delicate calibration
Birefringence	Tissue-scale stress	> 10 kPa	> s	μm	Global	Required flat, transparent sample; delicate calibration
Indentation/ Microplates/AFM	Cell or aggregate surface tension	0.1 Pa	s-hours	Few to 100 μm	Absolute measurements	Contact method
Pipette aspiration	Cell or aggregate surface tension	μN/m–mN/m	> 10 s	Few to 100 μm	Absolute measurements	Contact method
Subcellular laser ablation	Cell junction tension to dissipation ratio	NA	s–min	0.1−10 μm	Non-contact	Possible collateral damage
Force inference	Relative cell junction tension, cell pressure	NA	Video rate	> μm	Image based, global	Requires image segmentation

*Time scale of the mechanical processes that can be probed.

**Size scale of the mechanical processes or mechanical elements that can be probed.

which are made up of two components: a glomerulus and a tubule. Apart from common kidney deterioration conditions, in the case of lack of physical activities, especially in bedridden persons, the kidneys often bring suffering and are likely to develop tumors with severe consequences to the cardiovascular system. That is especially true as because, as mentioned before, the kidneys are connected to the aorta and the vena cava. To avoid such consequences, robotic rehabilitation with an appropriate bed is envisaged [17, 18]. For quality control, it is also suitable to use other imaging techniques, such as the pyelogram [19], already obsolete and uro Dyna-CT which, even though, provides high quality images [20]. Some metrics can be used for the purpose of the paper such as entropy [21], *power spectral density* (PSD) [22], percentage of *region of interest* (ROI) [23], and sinogram [24]. Entropy is actually an important metric reporting features included the image under test/processing. Let us consider a $m \times n$ image g having gray values $(x_1, x_2, x_3, \ldots, x_k)$; assuming $p(x_i)$ as the probability of each pixel value x_i in image g, it is possible to represent the amount of information encompassed within each pixel can be described as

$$q(x_i) = -p(x_i) \cdot \log p(x_i),\qquad(1)$$

for all the image g the total quantity of information will be obtained according to the following

$$Q(g) = -\sum_{i=1}^{k} q(x_i).\qquad(2)$$

Let us assume an image g to be segmented in n sub-regions $\langle r_i \rangle_{i=1}^{n}$, and the local entropy of each sub-region $Q(r_i)$ can be computed by means of (2). It is then possible to calculate the image

www.czasopisma.pan.pl PAN www.journals.pan.pl
POLSKA AKADEMIA NAUK

A. Lay-Ekuakille et al.: MEDICAL IMAGE MEASUREMENT AND CHARACTERIZATION: EXTRACTING MECHANICAL...

segmentation entropy Q_{1D} [25] as

$$Q_{1D} = \frac{\sum_{i=1}^{n} Q(r_i) - Q(g)}{Q(g)}. \tag{3}$$

Given the fact that segmentation entropy is based only on the pixel value itself, it is also denoted as 1-D image segmentation entropy. It exhibits the variation ratio of the entropy of segmented images comparing with the original image. Hence, generally a single pixel information of an image cannot exceed the ideal peak value. So, we can state that for most images, the larger Q_{1D} is, the more information from the segmented images we can obtain. Analogously, we can project the same analysis in 2-D since this latter overcomes limitations encountered in 1-D and, related to the fact Q_{1D} is not able to describe the random distribution of pixel values, it does not point out the strong correlation with its neighboring pixels. Q_{2D}, denoted as 2-D image segmentation entropy is able to overcome these issues given its ability to take into account both the pixel value itself and the average value of its eight neighboring pixels [26] encompassing two entropy parameters (x_i, y_j). Therefore, the 2-D image entropy $Q_{2D}(g)$ of the original image is

$$Q_{2D}(g) = -\sum_{i=1}^{k} \sum_{j=1}^{k} p_{ij} \cdot \log p_{ij}, \tag{4}$$

in which p_{ij} is the probability of each pixel in image g. The 2-D segmentation entropy, then, is

$$Q_{2D} = \frac{\sum_{i=1}^{n} Q_{2D}(r_i) - Q_{2D}(g)}{Q_{2D}(g)}. \tag{5}$$

As for the principle of 1-D image segmentation entropy, probabilities of most pixel values as well as their neighboring values are small. Thus, for most images, if the $Q_{2D}(g)$ is higher, more information will be obtained from these segmented images. A second indicator that can be used is the PSD with reference to stochastic process as it is in this paper. It is an important metric. Let us $X(t)$ a stochastic process in the time domain that is considered to be sampled over a finite interval of time $(-T/2; T/2)$ and denoted by $X_T(t)$. The Fourier transform of $X(t)$ is given by the following:

$$\widetilde{X}_T(f) = F\{X_T(t)\} = \int_{-\infty}^{\infty} X_T(t)e^{-2\pi ift}\,dt = \int_{-T/2}^{T/2} X(t)e^{-2\pi ift}\,dt. \tag{6}$$

The amplitude spectrum is the modulus of $\widetilde{X}_T$ and the phase spectrum is the argument of $\widetilde{X}_T$ although these are generally not informative for physical applications, if ever. The energy spectral density is found from $\widetilde{X}_T$ by finding the expectation of the squared amplitude spectrum:

$$E(f) = \varepsilon\left\{\left|\widetilde{X}_T(f)\right|^2\right\}. \tag{7}$$

We note the necessity for the onvergence mentioned previously: as T grows to infinity, so too does $E(f)$. We divide it by the interval length T to curb this growth which gives us an expression

for power spectral density:

$$S(f) = \lim_{T \to \infty} T^{-1} E(f) = \lim_{T \to \infty} \varepsilon \left\{ \frac{1}{T} \left| \int_{-T/2}^{T/2} X(t) e^{-2\pi i f t} \, dt \right|^2 \right\}, \tag{8}$$

which is real, non-negative, and exists for all stationary processes with zero mean and finite variance. Equation 6 defines the double-sided PSD, because in the limit of T, the limits of integration are $\pm\infty$. If $X(t)$ is real, the power spectrum $S(f)$ is even; hence, we only need estimates for $f \geq 0$. The single-sided PSD is thus given by $2S(f)$ for $f \geq 0$. We can translate the practical effect of 6 on a signal being processed as well as the image, too. The PSD, in its practical meaning, allows to the understand the filtering effect when we construct a bandpass filter. Hence, the energy outside the bandpass is zero. That is why we can express the PSD in W/Hz or in terms of wavelength. The *region of interest* (ROI) is usually expressed as a surface or area delimited by the interest of detecting a certain behavior of biological material under investigation.

The last indicator is the sinogram which comes from sinusoids produced to express a tomographic vision. Tomography allows to understand the different layers involved in the description of an item through imaging. We are interested to understand what happens inside the different spatial locations. Let us consider a function $f(x, y)$ which corresponds to a single pulse, as illustrated in Fig. 1a. If the pulse is set at the origin O, the projections measured by an observer will have a peak O' at the abscissa which is the projection of O on axis r, whatever the value of φ. If we report such projections in an image, that is a 3D plot, called a sinogram [27] that has as abscissa r and ordinate φ; along the third dimension, that is the grey level image, not reported in Fig. 1b, the value of the line integral of the function $f(x, y)$ should appear; this value is obtained by integrating along the line l as it is illustrated in Fig. 1a. If we imagine an illuminating candle, located at the origin, we get as image a vertical line at the abscissa 0 (the right $r = 0$ in Fig. 1b whose grey level is proportional to the luminosity of the candle. If, instead, we have three candles (luminous points within the image), the sinogram will exhibit a vertical track as before, other
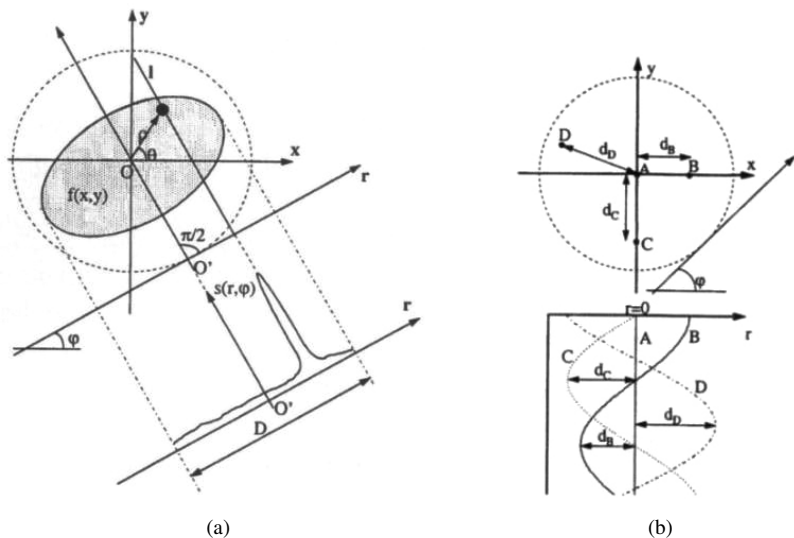

Fig. 1. Capturing external projections from outside an object (a) and graphical expression of a sinogram (b).

two tracks of sinusoidal shape, and a grey level proportional to the luminosity of the other two candles.

2. Mechanical and thermal stresses

Heat is transferred in human tissue and described by specific modeling, and among them we can find that proposed by Wulff [28], that is

$$\rho C_p \frac{\partial T}{\partial t} = k \frac{\partial^2 T}{\partial x^2} - \rho_b C_{pb} v \frac{\partial T}{\partial x} + Q_m, \tag{9}$$

where ρ is density (kg/m^3), C_p specific heat of the tissue (J/kg·K), T temperature (K, °C), t time (s), k thermal conductivity (W/m·K), ρ_b density of blood (kg/m^3), C_{pb} specific heat of the blood (J/kg·K), v is the local mean blood velocity (m/s), Q_m metabolic heat generation rate (W/m^3), subscript p indicates the index for coefficients of normalized PBHE (*Equivalence of Pennes Bioheat Equation*). Equation (9) can be solved with blood velocity v and the temperature is set as $T = T_a$ (external to tissue from outside) and $T = T_f$ (external to tissue as inside); the considered tissue, with for example a tumour, is in between and within two isothermal tissue boundaries. However, heat transfer in tissue requires a relaxation time (around 15–25 s) to accumulate sufficient energy to be transferred to a neighbouring item. In some cases, this time could be very short depending on the kind of tissue, notably epithelial, muscle, connective and nervous. The equation above does not consider micro-structural interactions, within the tissue, during heat transport transient process. Tzou [29] introduced a phase lag for temperature transient that leads to a *dual-phase lag* (DPL) model described as followings:

$$q(x, t + \tau_q) = -k \frac{\partial T(x, t + \tau_T)}{\partial x}, \tag{10}$$

in which T is the temperature, q the heat flux, k the thermal conductivity, x the distance and t the time. The phase lag of heat flux is τ_q and was used to interpret the short-time thermal inertia which induces the behaviour of the thermal wave. Mechanical stress, instead, could be measured by applying a dedicated instrumentation on a grasper system to assess the eventual trauma. Tissue under mechanical stress delivers a response due to a combination of its mechanical properties and environmental loading characteristics. Some authors [30] introduced the loading rate normalized in terms of the stress rate $\bar{\sigma}$ is an indicator for a potential metric that can be either measured or predicted for surgery by means of the monitoring of the current stress and position point (σ_i, x_i), and connected to previously recorded data n and m data points, and the associated time between points calculated as the number of data points multiplied by the sampling time step Δt, that is

$$\bar{\sigma} = \frac{\dfrac{\sigma_i - \sigma_{i-n})}{n \, \Delta t}}{\dfrac{(x_i - x_{i-m})}{m \, \Delta t}}. \tag{11}$$

Equation (11) exhibits the indicator called stress rate and it increases in the tissue and normalizes this with respect to the loading rate. Figure 2 depicts examples of different graspers used in surgery. They are traumatic and atraumatic.

Trying to minimize the impacts of thermal and mechanical stress on tissue, graspers' manufacturers have developed equipment able to mimic the human hand. They are generally called as
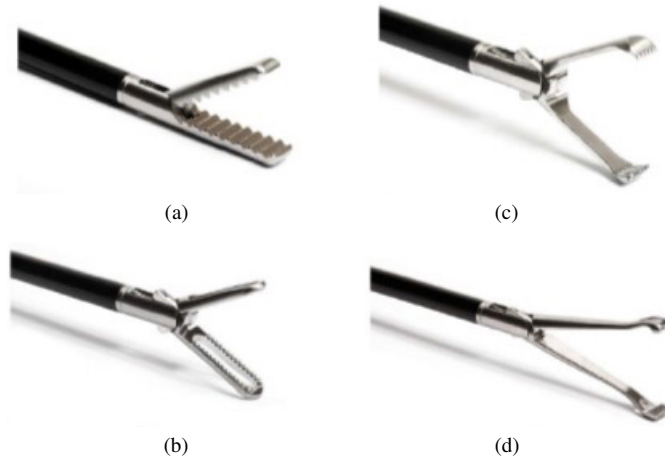
Fig. 2. Examples of reusable laparoscopic grasper: (a) crocodile-based forceps (traumatic), (b) short fenestrated (atraumatic), (c) fine toothed forceps (traumatic), and (d) babcock (atraumatic).

HALS (*hand-assisted laparoscopic surgery*) to be used for traditional and robotic interventions (see Fig. 3). These devices mostly allow all positions that a human hand can exhibit including opening.
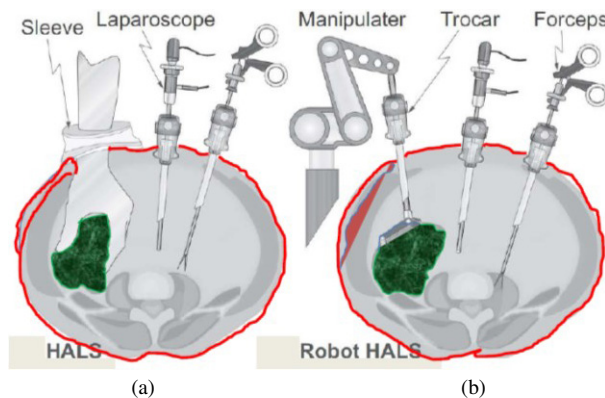

Fig. 3. The comparison between (a) conventional HALS and (b) robotic HALS.

3. Proposed method

Thermal and mechanical stress can be measured by means of infrared cameras and instrumented graspers for surgery. Since it is not easy to have different instruments connected to graspers and HALS due to the small space in surgery activities, an alternative approach which is the main motivation for this paper, can be adopted. It fits with augmented virtual reality. In other words, we have developed an approach based on determination of thermal and mechanical stresses by means of images to be acquired prior to surgical intervention and/or when it takes place (real time). The image processing for stresses has been developed in the Comsol environment [31, 32].

9

We used stationary modeling; The stationary study is used when field variables do not change over time. Here some examples. In electromagnetism, it is used to compute static electric or magnetic fields as well as direct currents. In heat transfer, it is used to compute the temperature field at thermal equilibrium. In solid mechanics, it is used to compute deformations, stresses, and strains at static equilibrium. In fluid flow it is used to compute the steady flow and pressure fields. In chemical species transport, it is used to compute steady-state chemical composition in steady flows. In chemical reactions, it is used to compute the chemical composition at equilibrium of a reacting system. We have chosen the parameters fitting with biological tissue, especially kidney, see Table 2.

Table 2. Tissue parameters specification.

Property	Name	Value
Thermal capacity at constant pressure	C_p	3 540
Density	ρ	1 079
Thermalconductivity	K	0.52
Frequency factor Activation	dE	257 700

The algorithm works according to the following steps: (i) implementing a GUI (graphic user interface), (ii) image conversion through a SolidWorks routine, (iii) image meshing, with creation of different gratings including small ones (iii), thermal and mechanical processing. Details of the algorithm are depicted in Fig. 4.
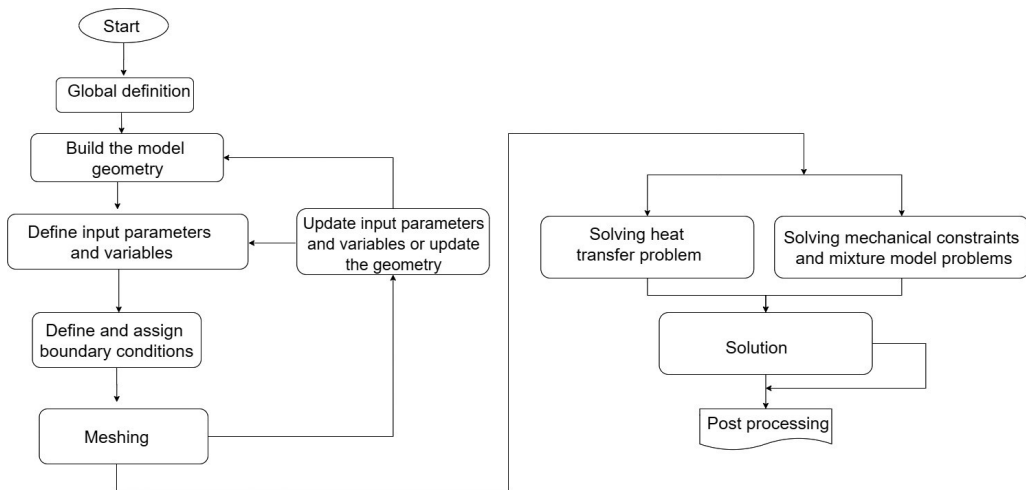

Fig. 4. Flowchart of the algorithm based on Comsol Environment processing.

We applied the approach to different images captured from surgery activity by means of a da Vinci Robot [33] that took place in the Hospital of Reggio Calabria at the beginning of 2019. A series of images have been processed. As an instance, we used two images of the same person suffering from kidney carcinoma of a, that is Figs. 5 and 6.
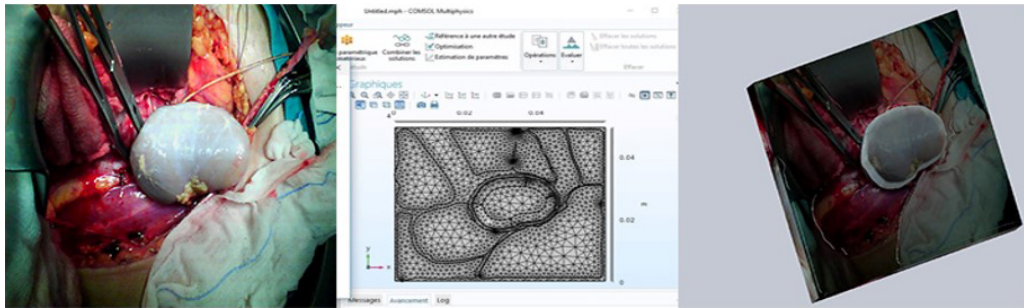
Fig. 5. First image meshing with related GUI (left and center) and its Solid Works implementation (right).
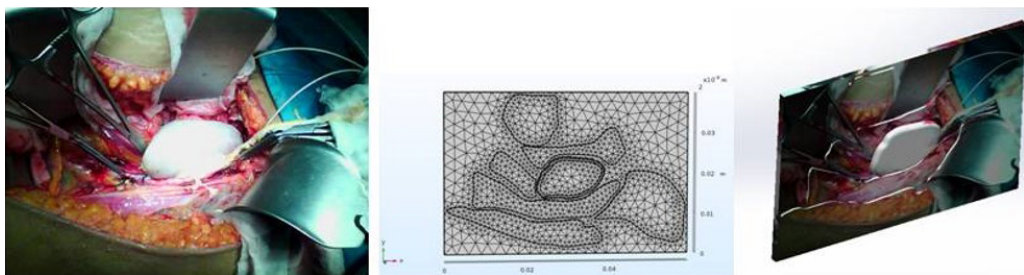

Fig. 6. Second image meshing with related GUI (left and center) and its Solid Works implementation (right).

Image meshing is implemented using dedicated information as per Table 3. This information is necessary for carrying out gratings. Note that the minimum growth rate has been set to 1.45 m. Actually, it is a fictitious value to see possible expansion of the tissue since the tissue dilatation is a matter of less than "mm".

Table 3. Meshing information.

Description	Value	Units
Maximum element quality	0.0048	m
Average element quality	0.0006	m
Minimum growth rate	1.45	m
Tiangular elements	1 280	Cst
Edge elements	0.5	Cst
Vortex elements	0.6	Cst

4. Results

The algorithm was applied ton surgery images of a person (over 65 years of age) suffering from kidney carcinoma of the. The main task was to evaluate the maximum threshold in terms of thermal and mechanical stresses exerted by graspers and other surgery tools. It is necessary to remind that the kidneys are involved in the following processes: filtration, re-absorption,

secretion, and excretion. Considering special connections with the aorta and the vena cava, any of the above processes renders the kidneys a pivotal organ within the human body. Any stress during surgery affects others organs. As indicated above, two images, out of many others, were used to demonstrate the importance of determining thermal and mechanical stress on this specific organ. Two series of processing were performed in this work. One is illustrated in Figs. 7 to 9 and the other in Figs. 10 to 12. Figure 7 illustrates the bio-heat (max $2.15 \times 10^1 \sim 16$ calories) and mechanical stress (max 8.010×10^1 N/m^2) generated by the contacts of surgery graspers and utensils. By comparing the results from Fig. 9 with analogous for the second image, we can see the bio-heat of the same order (max $1.00 \times 10^1 \sim 16$ calories), which is half and minor mechanical stress (max 3.985×10^1 N/m^2). Of course, mechanical stress can have a bio-heat impact as well. For such a delicate organ as the kidney, these values of stress must be under control, both in the case of a kidney to be used for transplantation or when it is supposed to work in the same body.
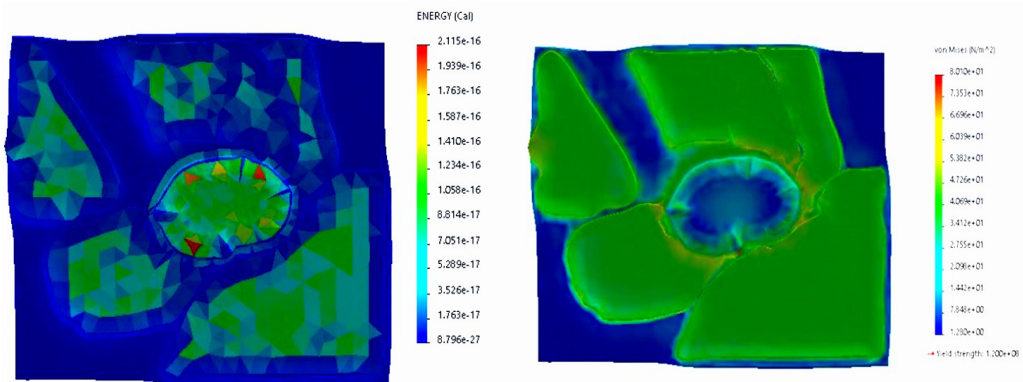

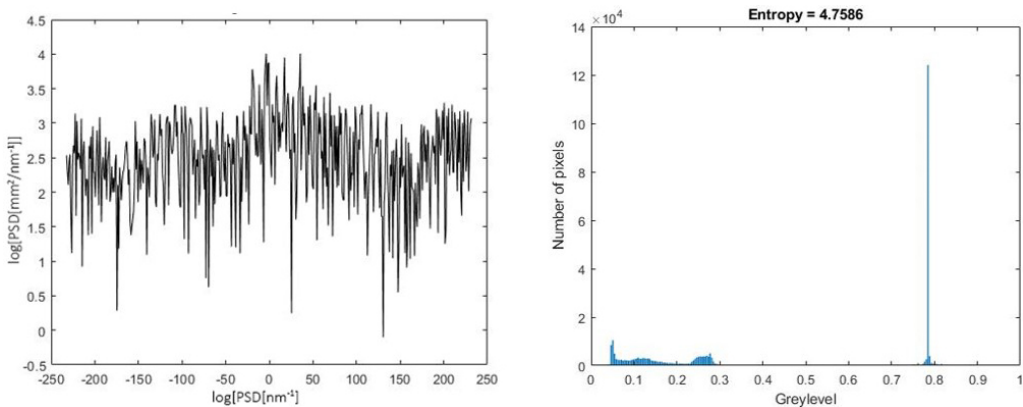Fig. 7. Thermal (left) and mechanical (right) stress for the first image.

Fig. 8. First image: power spectral density (left) and entropy (right).

Given the fact that both bio-heat and mechanical stress can be also monitored with instrumented devices, knowing specific indicators such as power spectral density (in Pa^2/Hz or dB) and entropy is essential in order to get confirmation of bio-heat and mechanical stress distribution.

Again, comparing PSDs (in Pa^2/Hz or dB), using Fig. 8 (right) and Fig. 10 (right), a little higher PSD is encountered within the first image that corresponds to as much stress. That is coherent with major thermal energy, then a major mechanical shock. Analogously, in terms of entropy, a peak is noticed at higher grey levels (Fig. 8 right) whilst in Fig. 10 (right) it is at a low level; which confirms that more energy has been deployed in the first image than in the second. In other words, the kidney in the first image emits more radiation than in the second one. The advantage of the present process, in real imaging, is that it can be employed on any instrumentation being able to capture inner energies, thermal and mechanical, emitted by human organ during surgery or other explorations. The kidney, as a pivotal organ, basically beahaves in the same way [34]. Once results of thermal and mechanical stress are available, surgeons can work on a database related to specific organs by listing patients' records such age, gender, activities (job), other pathologies, etc. This database will allow them to prevent unnecessary stress on organs. We reaffirm that this approach is vital to preserve organs to be trated and/or for transplantation.
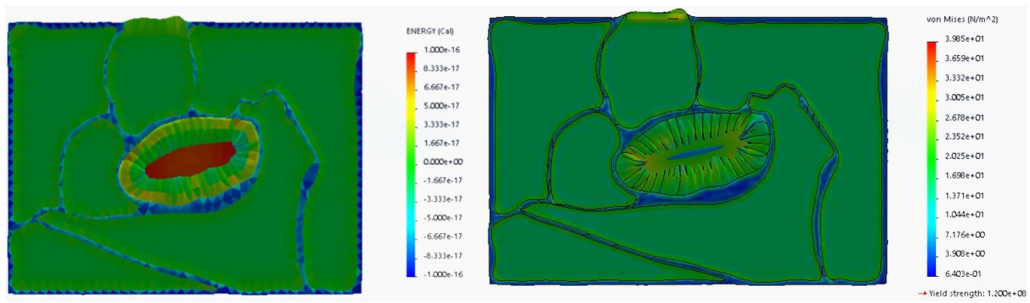

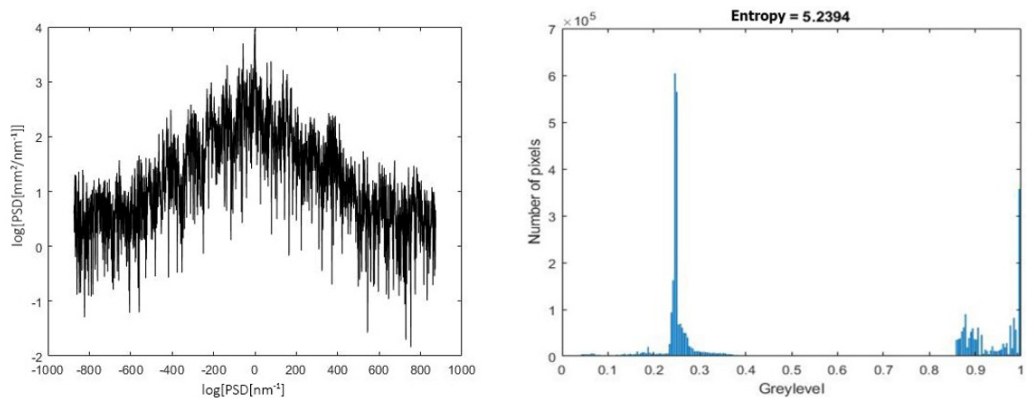Fig. 9. Thermal (left) and mechanical (right) stress for the second image.

Fig. 10. Power spectral density for the second image: 2-D (bottom) and 3-D (down).

The approach we have worked out will be especially exploited in the latter field i.e. organs to be donated to other people. Another important issue is the computational cost. The whole process, automatically guided, requires less than 2–3 minutes using a normal 64-bit netbook with 4 Gbytes of RAM.

13

5. Proposal of an innovating comparison

A further comparison is required to strengthen the aforementiond results. We use a computer vision approach for robotics by implementing a processing of both images through a monadic algorithm [35] in the effort to extract features. A monadic operation allows to process the levels of intensity of pixels of original input image by producing one output image. The algorithm, applying the suggested monadic operations, is shown in Fig. 11.
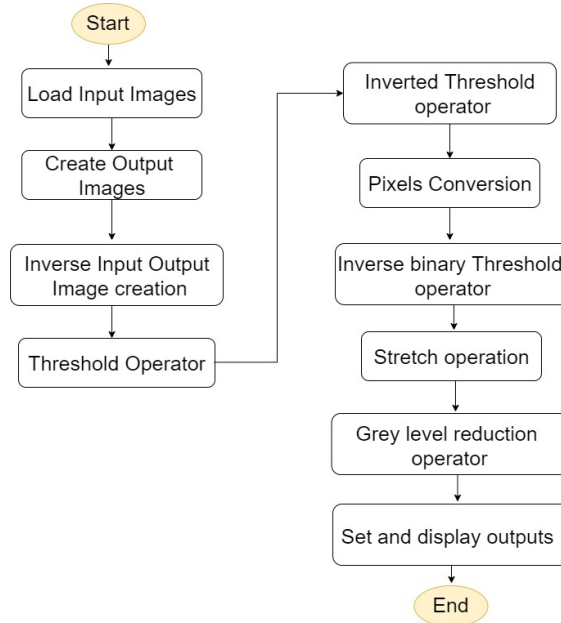

Fig. 11. Monadic algorithm steps.

This process is applied to both images and the results are shown in Figs. 12 and 13 respectively. The blue areas of both images indicate the propagation of both stresses, that is mechanical and thermal, in the other area of the the biological tissue not close to the points under surgery operations. Our approach is different in its being based on computer vision. It reflects the same area of the previous sections.

Whatever color is needed it can be produced by mixing three primary colors of light: red, green, and blue, each with its own intensity. The algorithm used [36] creates a simple image containing continuous areas of red, green, and blue using the MATLAB Image Processing Toolbox and then constructs an image for each of its distinct color planes (red, green, and blue). Basically, to perform image segmentation and object detection correctly, there is a need for images that are stable regardless of fluctuating imaging conditions. To reduce uniform color fields, the intensity normalization removes the shadow. This process uses a Lambertian reflector (12) operating under white illumination.

$$f^c(x) = m^b(x) \int_\omega s(\lambda, x)\rho^c(\lambda)\,\mathrm{d}\lambda,\qquad(12)$$

where $m^b(x)$ is the coefficient which denotes the relationship between the white light source and the surface reflectance, s and ρ are determined by the sensor and the surface of the object. It is
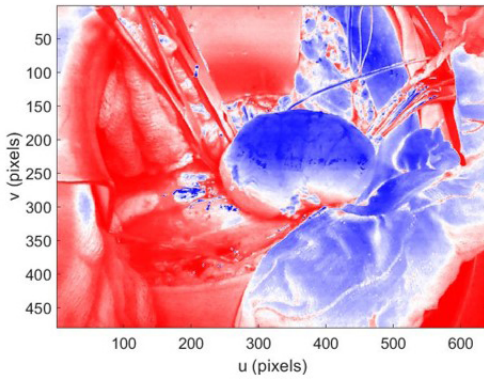
14

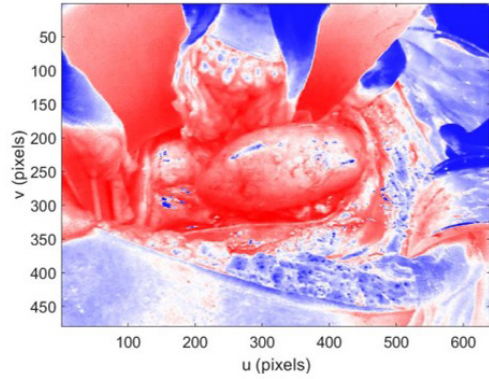Fig. 12. Monadic-based processing for the first image.   Fig. 13. Monadic-based processing for the second image.

important to notice that each separate colour plane in the figure contains an area of white. The white corresponds to the highest of each separate colour. For example, in the red plane image, the white represents the highest concentration of pure red values.

As red becomes mixed with green [37] or blue, gray pixels appear. The black region in the image shows pixel values that contain no red values, *i.e.*, $R = 0$. Figures 14 and 15 are, hence, the results of the process explained in (12). Different items encompassed in these images illustrate the use of different bands in order to point out the interested areas of stress. Figure 14 also depicts the histograms in different bands as well as the cumulative histogram. Instead, Fig. 15 shows the detailed masking process that also points out the stressed areas. Analogously, Figs. 16 and 17 show the same results for the second original image. To summarize the achievements, let us have
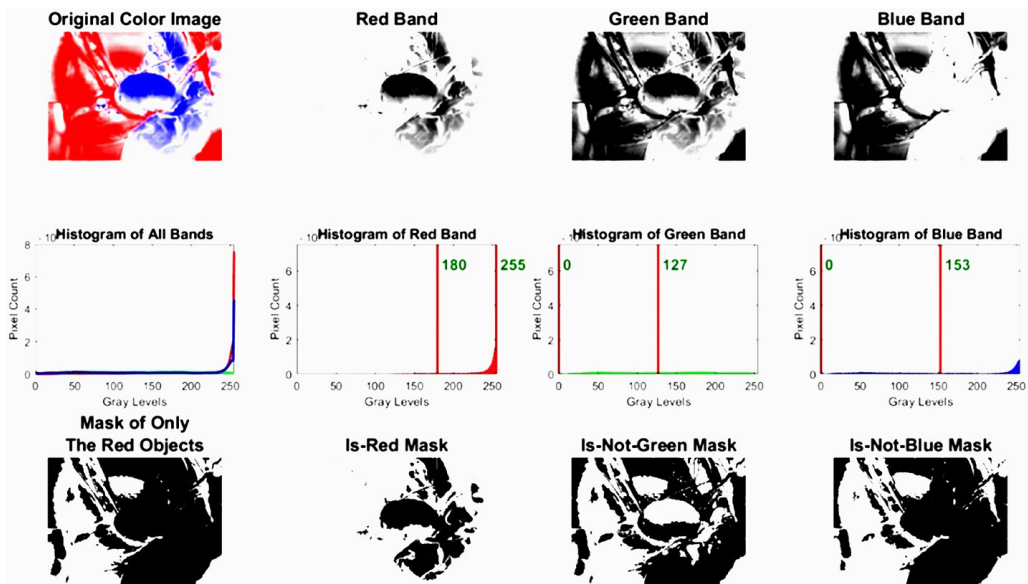

Fig. 14. A set of image processing results in different bands with histograms for the first image.

15

a look at Table 4 illustrating the detectability of the *region of interest* (ROI). We discriminate the core ROI, that is, the ROI in direct contact with the surgery instruments; the side ROI is an indirect region affected by side effect/after effect of the use of the considered instruments. This
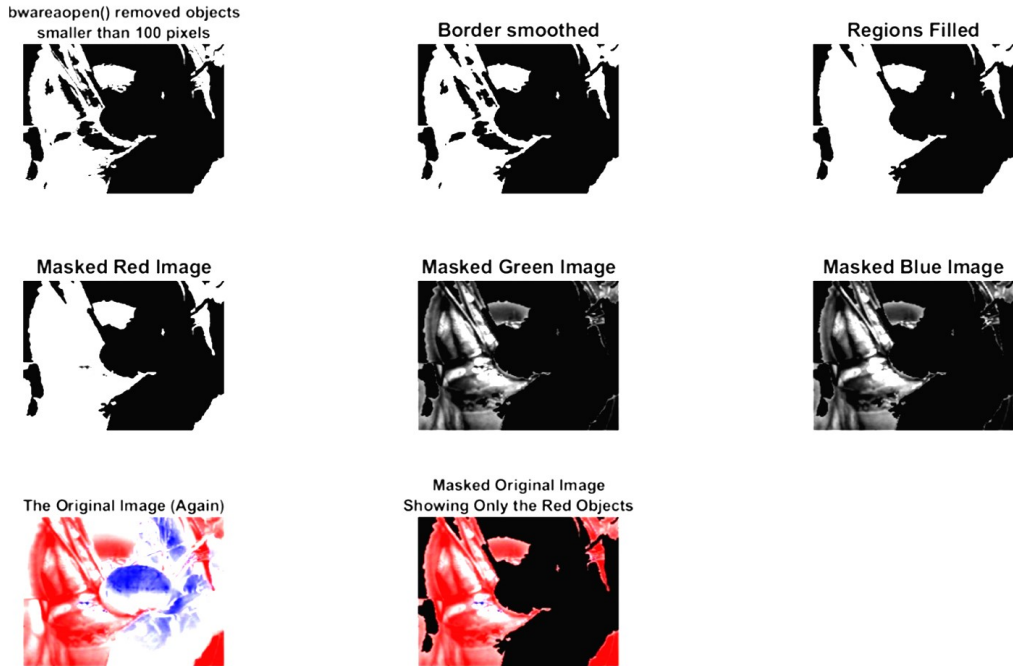

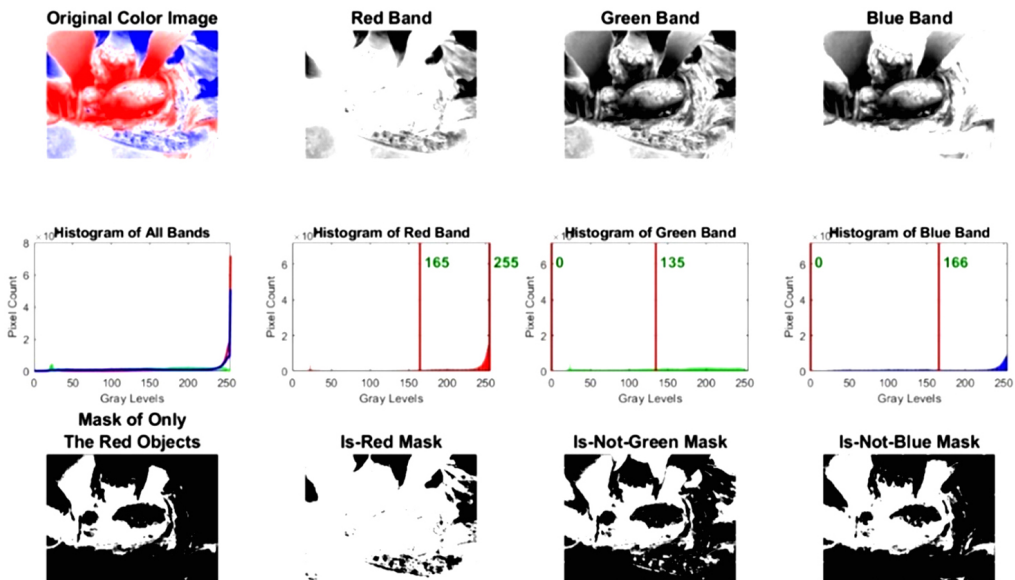Fig. 15. Details of the masking procedure in different bands for the first image.

Fig. 16. A set of image processing results in different bands with histograms for the second image.
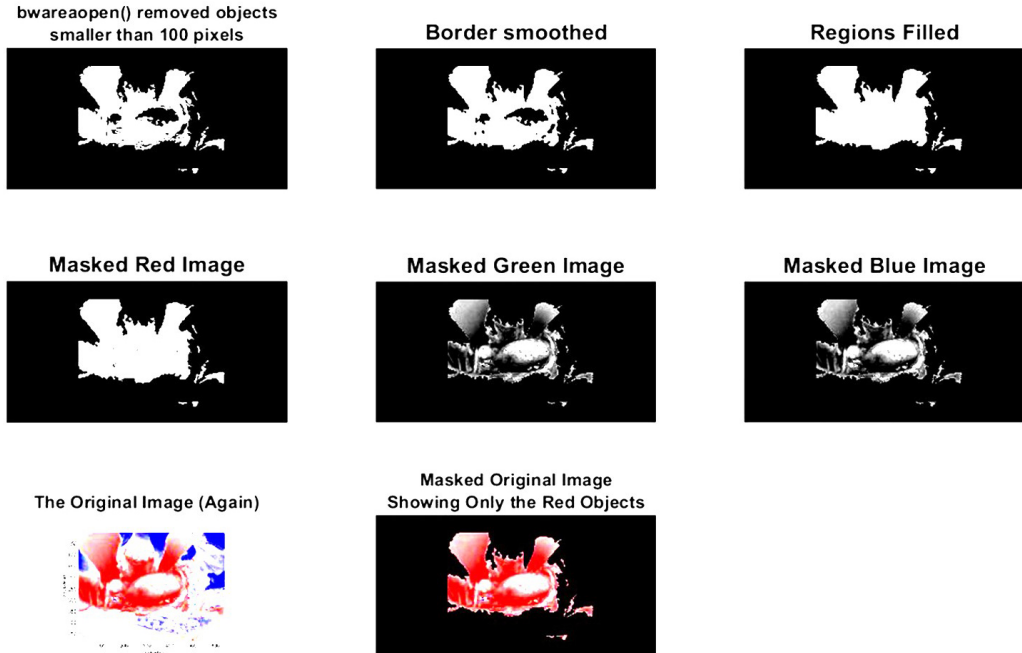
Fig. 17. Details of the masking procedure in different bands for the second image.

region could be impacted by a slight and physiological trauma. As we can notice, the Lambertian reflector illustrated in Figs. 14 to 17 is suitable for quantitative global detection. Conversely, it is difficult to use for core ROI detection. The results of combined Comsol-based modeling using bioheat equation and monadic-based processing are collected in Table 4.

Table 4. ROI target.

Image reference	Core ROI %	Side ROI %	Global ROI %	Technique/algorithm	Remarks
Image 1 thermal stress	5–8	12–15	17–23	Comsol modeling	
Image 2 thermal stress	10–12	13–15	23–27	Comsol modeling	
Image 1 mech. Stress	4–6	10–12	17–21	Comsol modeling	
Image 2 mech. Stress	7–8	10–12	14–18	Comsol modeling	
Image 1 monadic	15–17	42–44	57–61	Monadic operations	Blue
Image 2 monadic	3–4	54–56	57–60	Monadic operations	Blue
Image 1 multiband	Undetectable	Undetectable	68–70	Lambertian reflector	
Image 2 multiband	Undetectable	Undetectable	48–52	Lambertian reflector	

Further confirmation for supporting this approach is displayed by using the sinogram as explained in the introduction. Since we work with images in 3D, given the example of the three candles in the introduction, it works as though each of the candles illuminated the inner part of the human organ, that is the kidney, in order to get a vertical track, a sinusoidal shape, and grey levels proportional to the luminosity of the other two candles. In fact, in Fig. 18 (left), we can see

two lights on the sinusoid testifying to a concentrated distribution of the thermal and mechanical stresses, see also the trend of the PSD in Fig. 8 (left), whilst Fig. 18 (right) reports a little light diffusion, especially at the left, at the crossing of sinusoids that is in accordance with the trend of the PSD in Fig. 10 (left).
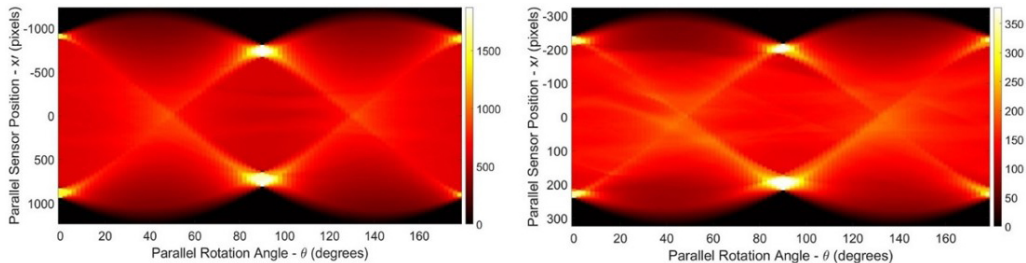

Fig. 18. Sinograms of monadic approach (Image 1 and 2 from the left to the right).

6. Conclusions

Human inner organs are subject to stress during surgery. These stresses, namely thermal and mechanical, are caused by the use of surgical instruments. In many cases, as reported in the introduction, these stresses can heavily affect the organ operated on and the neighborhood. Major attention has been requesting to address the issue. This latter has been becoming a topic of research due to two main reasons: (i) increasing request of insurance for surgeons to cover eventual damages during surgery, (ii) major awareness from biomedical devices manufacturers to lower level of risks by adopting new materials. Even though, it is necessary to pre-establish the right pressure to be exerted on the organ so that a taxonomy of pressure levels should be investigated. For now, thanks to this kind of research, it could be possible to capture images by means of sensing devices such external camera, and laparoscopy instruments, and to process them. The required time to retrieve all processed images included sinograms is around 45–50 seconds with a normal computer. It is an acceptable time for surgical operations lasting at least 30 minutes to deliver results for making decision. The research opens the path to possible research lines for instrumented graspers, forceps, and babcocks with dedicated sensors to allow the surgeons to calibrate the right pressure and subsequent thermal reactions. As we have seen, the sinograms are a double-face exhibition of results; that is, we can consider an observer/candle illuminating the inner part of an organ and/or tissue but also a way to pick and place virtual optical sensors for allowing us to understand the light concentration or diffusion. Moreover, thermal therapies [38,39] can utilize he approach followed in this paper. Noninvasive instrumental techniques, for capturing imaging for surgery decision-making, can be useful for allowing the modeling of thermal and mechanical stresses. Predicting stress is useful in all kind of surgical activities and in particular in robotic one where it is possible to preset the necessary load on tissues. The research also falls in the *augmented virtual reality* (AVR) as subsequent step.

References

[1] Lay-Ekuakille, A., Visconti, P., de Fazio, R., & Veneziano, D. (2019). Quasi-real time acquisition and processing for biomedical IR and conventional imaging in surgery applications, *Journal of Instrumentation*, *14*(3). https://doi.org/10.1088/1748-0221/14/03/P03011

[2] Cheng, L., & Hannaford, B. (2016). Evaluation of liver tissue damage and grasp stability using finite element analysis. Computer Methods in Biomechanics and Biomedical Engineering, *19*(1), 31–40. https://doi.org/10.1080/10255842.2014.981166

[3] Cartmill, J. A., Shakeshaft, A. J., Walsh, W. R., & Martin, C. J. (1999). High pressures are generated at the tip of laparoscopic graspers. *Australian and New Zealand Journal of Surgery*, *69*(2), 127–130. https://doi.org/10.1046/j.1440-1622.1999.01496.x

[4] Van der Voort, M., Heijnsdijk, E. A. M., & Gouma, D. J. (2004). Bowel injury as a complication of laparoscopy. *British Journal of Surgery*, *91*(9), 1253–1258. https://doi.org/10.1002/bjs.4716

[5] Tang, B., Hanna, G. B., Joice, P., & Cuschieri, A. (2004). Identification and categorization of technical errors by Observational Clinical Human Reliability Assessment (OCHRA) during laparoscopic chole-cystectomy, *Archives of Surgery*, *139*(6), 1215–1230. https://doi.org/10.1001/archsurg.139.11.1215

[6] Dargahi, J., Najarian, S., & Najarian, K. (2005). Development and three-dimensional modelling of a biological-tissue grasper tool equipped with a tactile sensor, *Canadian Journal of Electrical and Computer Engineering*, *30*(3), 225–230. https://doi.org/10.1109/CJECE.2005.1541755

[7] De, S., Rosen, J., Dagan, A., Hannaford, B., Swanson, P., & Sinanan, M. (2007). Assessment of Tissue Damage due to Mechanical Stresses, *The International Journal of Robotics Research.*, *26*(6), 1159–1171. https://doi.org/10.1177/0278364907082847

[8] Bicchi, A., Canepa, G., De Rossi, D., Iacconi, P., & Scillingo, E. P. (1996, April). A sensor-based minimally invasive surgery tool for detecting tissual elastic properties (003) 5323219. *Proceedings of IEEE International Conference on Robotics and Automation*, USA, *1*, 884–888. https://doi.org/10.1109/ROBOT.1996.503884

[9] Heijnsdijk, E. A. M., De Visser, H., Dankelman, J., & Gouma, D. J. (2004). Slip and damage properties of jaws of laparoscopic graspers. *Surgical Endoscopy and Other Interventional Techniques*, *18*(5), 974–979. https://doi.org/10.1007/s00464-003-9153-2

[10] Lay-Ekuakille, A., Vergallo, P., Jabłoński, I., Casciaro, S., & Conversano, F. (2016). Measuring Lung Abnormalities in Images-based CT. *International Journal on Smart Sensing and Intelligent Systems*, *9*(2), 1156–1179. https://doi.org/10.21307/ijssis-2017-912

[11] Gómez-González, M., Latorre, E., Arroyo, M., & Trepat, X. (2020). Measuring mechanical stress in living tissues. *Nature Reviews Physics 2*, 300–317. https://doi.org/10.1038/s42254-020-0184-6

[12] Fung, Y. C. (1993). *Biomechanics: Mechanical properties of living tissues*. Springer. https://doi.org/10.1007/978-1-4757-2257-4

[13] Oates, A. C., Gorfinkiel, N., González-Gaitán, M., & Heisenberg, C. P. (2009). Quantitative approaches in developmental biology. *Nature Reviews Genetics,* 10, 517–530. https://doi.org/10.1038/nrg2548

[14] Sugimura, K., Lenne, P. F., & Graner, F. (2016). Measuring forces and stresses in situ in living tissues. *Development*, *143*, 186–196. https://doi.org/10.1242/dev.119776

[15] Addae-Mensah, K. A., & Wikswo, J. P. (2008). Measurement techniques for cellular biomechanics in vitro. *Experimental Biology and Medicine*, *233*, 792–809. https://doi.org/10.3181/0710-MR-278

[16] Choi, D. K., & Koo, D. (2017). A study on real-time stress calculation of soft tissues using digital image techniques, *Journal of Biomechanical Science and Engineering*, *12*(1), 2–13. https://doi.org/10.1299/jbse.16-00607

[17] Chiffi, C., & Lay-Ekuakille, A. (2016). Physiotherapeutic Movements by Advanced Robotic Beds: Perspectives in Triggering Nanodrugs. *2016 Nanotechnology for Instrumentation and Measurement (NANOfIM)*, Germany, 5–16. https://doi.org/10.1109/NANOFIM.2016.8521420

[18] Harvey, L. A. (2016). Physiotherapy rehabilitation for people with spinal cord injuries. *Journal of Physiotherapy*, *62*(1), 4–11. https://doi.org/10.1016/j.jphys.2015.11.004

[19] Pooli, A., Brush, T., Belle, J. D., & LaGrange, C. A. (2017). Delayed severe anaphylactoid reaction following retrograde pyelogram: A case report. *SAGE Open Medical Case Reports*, 5, 2050313X17745212. https://doi.org/10.1177/2050313X17745212

[20] Ritter, M., Rassweiler, M. C., & Michel, M. S. (2015). The Uro Dyna-CT enables three-dimensional planned laser-guided complex punctures. *European Urology*, 68(4), 880–884. https://doi.org/10.1016/j.eururo.2015.07.005

[21] Bhateja, V., Patel, H., Krishn, A., Sahu, A., & Lay-Ekuakille, A. (2015). Multimodal medical image sensor fusion framework using cascade of wavelet and contourlet transform domains. *IEEE Sensors Journal*, 15(11), 6783–6790. https://doi.org/10.1109/JSEN.2015.2465935

[22] Giorgio, G. A., Ragosta, M., & Telesca, V. (2017). Application of a multivariate statistical index on series of weather measurements at local scale. *Measurement*, 112, 61–66. https://doi.org/10.1016/j.measurement.2017.08.005

[23] Lin, H., Si, J., & Abousleman, G. P. (2007, April). Region-of-interest detection and its application to image segmentation and compression. *2007 International Conference on Integration of Knowledge Intensive Multi-Agent Systems*, USA, 306–311. https://doi.org/10.1109/KIMAS.2007.369827

[24] Prince, J. L., & Willsky, A. S. (1993). Hierarchical Reconstruction using Geometry and Sinogram Restoration", *IEEE Transactions on Image Processing*, 2(3), 401–416. https://doi.org/10.1109/83.236529

[25] Chen, X., Wang, R., Cao, Y., Yu, W., & Feng, J. (2012). A novel evaluation method based on entropy for image segmentation. *Procedia Engineering*, 29, 3959–3965. https://doi.org/10.1016/j.proeng.2012.01.602

[26] Sparavigna, A. C. (2019). Entropy in Image Analysis. *Entropy*, 21(4), 1–4. https://doi.org/10.3390/e21050502

[27] Lanzavecchia, S., Tosoni, L., & Bellon, P. L. (1996). Fast sinogram computation and the sinogram-based alignment of images. *Computer applications in the biosciences: CABIOS*, 12(5), 531–537. https://doi.org/10.1093/bioinformatics/12.6.531

[28] Das, K. & Mishra, S. C. (2014). Study of thermal behavior of a biological tissue: An equivalence of Pennes bioheat equation and Wulff continuum model. *Journal of Thermal Biology*, 45, 103–109. https://doi.org/10.1016/j.jtherbio.2014.08.007

[29] Tzou, D. Y., Beraun, J. E., & Chen, J. K. (2002). Ultrafast deformation in femtosecond laser heating. *Journal of Heat Transfer*, 124(2), 284–292. https://doi.org/10.1115/1.1447934

[30] Chandler, J. H., Mushtaq, F., Moxley-Wyles, B., West, N. P., Taylor, G. W., & Culmer, P. R. (2017). Real-time assessment of mechanical tissue trauma in surgery. *IEEE Transactions on Biomedical Engineering*, 64(9), 2384–2393. https://doi.org/10.1109/TBME.2017.2664668

[31] Juch, T. (2014, August 2). *Bioheat Transfer, Heat Flux* [Online forum post]. Comsol. https://www.comsol.com/forum/thread/46501/bioheat-transfer-heat-flux

[32] COMSOL. *Application Gallery*. Retrieved March 9, 2020, from https://www.comsol.com/models/structural-mechanics-module

[33] Intuitive. *Kidney Surgery. Learn about kidney cancer surgery and understand your options.* Retrieved March 22, 2020, from https://www.davincisurgery.com/procedures/urology-surgery/kidney-surgery

[34] Yifeng, P., Zehua, Z., Guohao, D., Tiqiao, X., Hongjie, X., & Peiping, Z. (2013). Experimental investigation of mouse kidney aging with SR PCI technology. *Journal of Instrumentation, 8*, C08004. https://doi.org/10.1088/1748-0221/8/08/C08004

[35] Scott, R. G., Navarro Leija, O. S., Devietti, J., & Newton, R. R. (2017). Monadic composition for deterministic, parallel batch processing. *Proceedings of the ACM on Programming Languages*, 73. https://doi.org/10.1145/3133897

[36] Linhares, J. M., Monteiro, J. A., Bailão, A., Cardeira, L., Kondo, T., Nakauchi, S., Picollo, M., Cucci C., Casini, A., Stefani, L. & Nascimento, S. M. C. (2020). How Good Are RGB Cameras Retrieving Colors of Natural Scenes and Paintings? – A Study Based on Hyperspectral Imaging. *Sensors*, *20*(21), 6242. https://doi.org/10.3390/s20216242

[37] Image Analyst. (2020). *SimpleColorDetection()*. MATLAB Central File Exchange. Retrieved December 7, 2020, from https://www.mathworks.com/matlabcentral/fileexchange/26420-simplecolor detection

[38] Singh, J., Gupta, P. K., & Rai, K. N. (2011). Solution of fractional bioheat equations by finite difference method and HPM. *Mathematical and Computer Modelling*, *54*(9-10), 2316–2325. https://doi.org/10.1016/j.mcm.2011.05.040

[39] Soloperto, G., Conversano, F., Greco, A., Casciaro, E., Ragusa, A., Lay-Ekuakille, A., & Casciaro, S. (2013). Assessment of the Enhancement Potential of Halloysite Nanotubes for Echographic Imaging. *2013 IEEE International Symposium on Medical Measurements and Applications (MeMeA)*, Canada. https://doi.org/10.1109/MeMeA.2013.6549700

Aimé Lay-Ekuakille has been with the Dept. of Innovation Engineering, University of Salento, Italy since 2000, and is the Director of Instrumentation and Measurement Lab I. Prof. Aimé Lay-Ekuakille is a Senior Member of the IEEE. His main areas of research are: (i) Instrumentation and Measurements for Biomedical, Environmental and Industrial applications, (ii) Sensors and Sensing Systems, (iii) Nanotechnology, (iv) Artificial intelligence for Instrumentation and Measurement, and (v) Ageing and Characterization of Photovoltaic Panels. He has authored and co-authored more than 300 papers on indexed international conferences and journals, as well as five international books. He serves as Senior Editor of the IEEE Transactions on Nanobioscience, the Editor of Measurement Journal (Elsevier, NL), Editor of the Measurement: Sensors (Elsevier, NL), Associate Editor of the IEEE Sensors Journal (USA).

Dr Satya P. Singh, received a B.Tech. in Electronics & Telecommunications Engineering from the Institution of Electronics & Telecommunication Engineers, New Delhi, M.Tech from J.C. Bose University of Science & Technology, YMCA, Faridabad, Haryana, India, and Ph.D in Electrical Engineering from Gautam Buddha University, Gr. Noida, India. Currently he is with the Nanyang Technological University in Singapore. His areas of research are artificial Intelligence, Machine Learning and Deep Learning, Instrumentation and Measurements.

Moise Avoci Ugwiri received both B.D in Electromechanical Engineering and M.D. in Applied Mechanics Engineering from the ISTA University (D.R. Congo). He is currently a Ph.D. student at the Industrial Department of the University of Salerno (Italy). His area of research is measurement for industrial applications, in particular, signal processing and Fault Detection. He is also currently working on robotics for medical applications. He is a member of IEEE IMS.

Md. Zia Ur Rahman (M'09–SM'16) received his M.Tech. and Ph.D. degrees from Andhra University, Visakhapatnam, India. He is currently a Professor with the Department of Electronics and Communication Engineering, K. L. University, Vaddeswaram, India. He has several publications in various journals and proceedings. His current research interests include adaptive signal processing, biomedical signal processing, array signal processing, MEMS, and nanophotonics. Dr. Ur Rahman is an Editor/Associate Editor/Editorial Board Member for various journals.

Prof. Consolatina Liguori Ph.D. in Industrial Engineering, she has been a Full Professor of Electrical and Electronic Measurements at the University of Salerno since 2012. Her current research interests include smart metering, image-based measurement systems and digital signal processing, measurement characterization, and instrument fault detection and isolation. From 2016, she has been a guest professor at the STC Research Centre (Mid Sweden University) within the field of electronic measurement system. She is a cofounder of three spin off companies of the UNISA: "SPRING OFF srl", "Metering Research srl" and "Hippocratica Imaging.

Domenico Veneziano is a Urologist, Fellow of the European Board of Urology. He was born in Reggio Calabria, Italy, were he actually works as a full-time physician in the department of Urology and Kidney Transplant, G.O.M. Hospital. His main fields of interest are oncologic mini-invasive surgery, urinary tract stone treatment and surgical education. In 2014 he completed a fellowship at the University of Minnesota in "simulation and education technologies" with the accreditation of the American College of Surgeons, one of the first fellowships in the world expressively dedicated to simulation in surgery. D. Veneziano is an internationally recognized expert in curriculum building, simulator design and in the organization of hands-on training events, with over 60 invited lectures since 2014.